Fall 2016

Currents- and varifolds-based registration of lung vessels and lung surfaces

Yue Pan
University of Iowa

CURRENTS- AND VARIFOLDS-BASED REGISTRATION OF LUNG VESSELS AND LUNG SURFACES

by

Yue Pan

A thesis submitted in partial fulfillment of the
requirements for the Master of Science
degree in Electrical and Computer Engineering
in the Graduate College of
The University of Iowa

December 2016

Thesis Supervisor: Professor Gary E. Christensen

Graduate College
The University of Iowa
Iowa City, Iowa

CERTIFICATE OF APPROVAL

MASTER'S THESIS

This is to certify that the Master's thesis of

Yue Pan

has been approved by the Examining Committee for the thesis requirement for the Master of Science degree in Electrical and Computer Engineering at the December 2016 graduation.

Thesis committee: _____
Gary E. Christensen, Thesis Supervisor

_____
Punam K. Saha

_____
Oguz C. Durumeric

_____
Geoffrey D. Hugo

ACKNOWLEDGEMENTS

First and foremost, I would like to show my deepest gratitude to my supervisor Professor Gary E. Christensen of Electrical and Computer Engineering and Radiation Oncology Department at the University of Iowa. He is a respectable, responsible and resourceful scholar, who has provided me with valuable guidance, impressive kindness and patience. His wide academic knowledge in many areas such as engineering, medical and math, inspired me a lot. His keen and vigorous academic observation enlightens me not only in this thesis, but also my future Ph.D study.

I shall extend my thanks to Dr. Geoffrey D. Hugo at Virgina Commonwealth University, who taught me a lot of medical knowledge to help me better understand my project and broaden my horizons. I also want to express my sincere appreciation to Professor Oguz C. Durumeric of Math Department at the University of Iowa. His clearly explanation and logic thinking enable me to understand math in a higher level.

At the same time, I want to thank all the incredible instructors of those engineering and math courses I have took, like Professor Hans Johnson, Professor Mathews Jacob, Professor Maggy Tomova and Professor Punam K. Saha etc., who equipped me with useful academic skills for my research.

Also, I am very glad I have a lot of excellent colleagues and friends, who gave me invaluable help. I want to express my gratitude to Wei Shao, Christopher Guy, Dakai Jin, Bowen Zhao, Joo Hyun Song, Sarah E. Gerard and Professor. Joseph M. Reinhardt. Working with them make my life much easier.

Last but not least, I want to thank my parents, Zhiqiang Pan and Liyi Zhai, and my boyfriend Siyang Tao. Thanks to their everlasting and unconditional love and supports, I feel stronger and more powerful.

Genius only means hard-working all one's life. (Mendeleyev Russian chemist)

This work was supported in part by the National Cancer Institute under award numbers R01CA166119 and R01CA166703. The content is solely the responsibility of the authors and does not necessarily represent the official views of the National Institutes of Health.

ABSTRACT

This thesis compares and contrasts currents- and varifolds-based diffeomorphic image registration approaches for registering tree-like structures in the lung and surface of the lung. In these approaches, curve-like structures in the lung—for example, the skeletons of vessels and airways segmentation—and surface of the lung are represented by currents or varifolds in the dual space of a Reproducing Kernel Hilbert Space (RKHS). Currents and varifolds representations are discretized and are parameterized via of a collection of momenta. A momenta corresponds to a line segment via the coordinates of the center of the line segment and the tangent direction of the line segment at the center. A momentum corresponds to a mesh via the coordinates of the center of the mesh and the normal direction of the mesh at the center. The magnitude of the tangent vector for the line segment and the normal vector for the mesh are the length of the line segment and the area of the mesh respectively. A varifolds-based registration approach is similar to currents except that two varifolds representations are aligned independent of the tangent(normal) vector orientation. An advantage of varifolds over currents is that the orientation of the tangent vectors can be difficult to determine especially when the vessel and airway trees are not connected. In this thesis, we examine the image registration sensitivity and accuracy of currents- and varifolds-based registration as a function of the number and location of momenta used to represent tree like-structures in the lung and the surface of the lung. The registrations presented in this thesis were generated using the Deformetrica

software package, which is publicly available at www.deformetrica.org.

PUBLIC ABSTRACT

Registration of lung CT images is important for many radiation oncology applications including assessing and adapting to anatomical changes, accumulating radiation dose for planning or assessment, and managing respiratory motion. For example, variation in the anatomy during radiotherapy introduces uncertainty between the planned and delivered radiation dose and may impact the appropriateness of the originally-designed treatment plan. Frequent imaging during radiotherapy accompanied by accurate longitudinal image registration facilitates measurement of such variation and its effect on the treatment plan. The cumulative dose to the target and normal tissue can be assessed by mapping delivered dose to a common reference anatomy and comparing to the prescribed dose. The treatment plan can then be adapted periodically during therapy to help mitigate the impact of these changes by ensuring the cumulative delivered dose is concordant with the prescribed dose[16, 10, 18]. Furthermore, image registration can also help measure how the tumor changes during or after treatment, which can potentially assist in predicting early response to therapy. These applications all rely on accurate tracking of lung motion over the breathing cycle and anatomical and functional changes over time.

The main contribution of this thesis is a sensitivity analysis of the feature-based (currents- and varifolds-based) image registration methods to learn how to choose good parameters for the algorithm and parametrize lung features in the lung, such as the centerline of the pulmonary vessel and airway trees, and surface of the

lung.

TABLE OF CONTENTS

LIST OF TABLES

Table

LIST OF FIGURES

Figure

CHAPTER 1
INTRODUCTION

Registering lung CT images is an important problem for many applications including tracking lung motion over the breathing cycle, tracking anatomical and function changes over time, and detecting abnormal mechanical properties of the lung.

Accurate image registration is critical for clinical study. However, the ability of an algorithm to match anatomy throughout the lung may be limited by the complex variations in the anatomy and limited image contrast. One approach to improving registration accuracy is to highlight and extract known anatomy such as pulmonary airways or blood vessels[3] to improve the matching at these tissue locations.

Image registration correspondence can be defined either through intensity-based or feature-based approaches. Intensity-based approaches register images by minimizing differences in intensities between the moving (deformed template) and target images. In general, intensity-based registration approaches have the advantage of not needing user intervention but often do a poor job of aligning features such as points, lines and surfaces contained in the images. Feature-based approaches are attractive because they directly match features, but they often require *a priori* point-to-point correspondence, which can be challenging in radiotherapy applications where this is often not known. Current- and varifold-based image registration are feature-based registration approaches with the advantage that no point correspondence is assumed between the objects being registered ([17],[6],[7]). The currents framework

has been successfully applied to perform registrations of MR images ([17],[5],[6]) and also lung CT images ([9]). A varifold-based registration approach [4] is similar to current-based registration approach except that two varifold representations can be aligned in an orientation invariant manner which will be discussed in the next section.

Current- and varifold-based image registration is built using the Large Deformation Diffeomorphic Metric Mapping (LDDMM) framework ([14],[15]). This framework produces correspondence maps (transformations) between images that are guaranteed to be diffeomorphisms.[1] In this work, the velocity field of the LDDMM framework is represented by currents ([5]) and the control points of the deformation field are not necessarily dense in order to get desired registration results ([6],[8]).

The contribution of this paper is a sensitivity analysis of the current- and varifold-based image registration methods to the number and location of momenta representing tree-like structures, such as the centerline of the pulmonary vessel and airway trees, and surface in the lung.

[1] A diffeomorphism is a bijective, differentiable map between two manifolds such that its inverse is also differentiable.

CHAPTER 2
METHODS

Currents and varifolds are mathematical objects that can be used to model general geometrical objects. A current is a linear functional on the space of compactly supported differential k-forms , on a smooth manifold which is continuous in the sense of distributions. Any set of curves or surfaces can be represented in terms of currents and also varifolds. The advantage of using currents and varifolds to register images is that the similarity measure is defined in the space of currents or varifolds, which does not assume any kind of point-correspondence between structures. A varifold can be considered a generalization of the idea of a current in the sense that the tangent vector of its representative momenta are not oriented. Theoretically, varifolds are weaker objects than currents due to the lack of orientation of the tangent vector of the momenta used to represent a shape. However, this "weaker" side of varifolds is a desirable property when matching line segments with uncertain tangent orientation.

2.1 Currents Representation

2.1.1 Curve Currents Representation

The current representation of a curve L is defined by the path/line integral along the curve through a test vector field ω via

$$L(\omega) = \int_L \omega(x)^t \tau(x) d\lambda(x) \tag{2.1}$$

where, τ is the tangent of the curve at point x and $d\lambda$ is the Lebesgue measure on the curve[9]. The test vector field ω is an element of a space of possible vector fields

W, where W is a Reproducing Kernel Hilbert Space (RKHS). In this work, W is a space of square integrable vector fields convolved with a smoothing Gaussian kernel: $\omega(x) = K^W(x,.)\alpha$, where the pair (x,α) is called a momentum. The tangent vector along the curve gives a natural action of the curve on vector fields. The norm of the current is defined in the dual space (currents space) W^* of W. W is a closed span of the vector fields $\omega(x) = K^W(x,.)\alpha$. The dual space of W denoted as W^* is a closed span of Dirac delta currents δ_x^α, where a Dirac delta current is the dual representation of the basis vector field $K^W(x,.)\alpha$. Based on the Riesz representation theorem[1], there is a linear mapping between W and its dual space W^*, $\mathcal{L}_W : W \to W^*$ such that

$$\mathcal{L}_W(\omega)(\omega') =< \omega, \omega' >_W \tag{2.2}$$

where $<,>_W$ denotes inner prodcut of the RKHS, i.e., $\mathcal{L}_W$ maps a vector filed ω to a corresponding current and the current $\mathcal{L}_W(\omega)$ is an operator itself, which operates on a vector field.

Therefore, $\delta_x^\alpha = \mathcal{L}_W(K^W(x,.)\alpha)$

In a discrete setting, curves may be represented as polygonal lines(a connected series of line segemtns) where the direction of the tangent is constant over each line segment. In this case, the current representation of a polygonal curve is given by

$$L(\omega) = \sum_k \omega(x_k)^t \tau(x_k) \tag{2.3}$$

where x_k is the center of each line segment and $\tau(x_k)$ is the tangent vector at x_k. The

[1]This theorem establishes an important connection between a Hilbert space and its (continuous) dual space. If the underlying field is the real numbers, the two are isometrically isomorphic.

magnitude of $\tau(x_k)$ is proportional to the length of the line segment centered at x_k.

2.1.2 Surface Currents Representation

The current representation of a surface S is defined by the flux integral through a test vector field ω via

$$S(\omega) = \int_S \omega(x)^t n(x) d\lambda(x) \tag{2.4}$$

where, n is the unit normal of the surface at point x and $d\lambda$ is the Lebesgue measure on the surface. The test vector field ω is an element of a space of possible vector fields W, where W is a Reproducing Kernel Hilbert Space (RKHS).

Similar as curve currents, in discrete setting the continuous current equation of surface Eq. 2.4 can be replaced by:

$$S(\omega) = \sum_k \omega(x_k)^t n(x_k) \tag{2.5}$$

where x_k is the center of each mesh and $n(x_k)$ is the normal vector at x_k[9]. The magnitude of $n(x_k)$ is proportional to the area of the mesh centered at x_k.

2.2 Diffeomorphic Deformation Framework

2.2.1 Currents Framework

We first describe the image registration cost function for two curves represented by currents. Let L_1 and L_2 be two curves that we want to register. Each curve is mapped to its dual space currents representation denoted as T_1 and T_2, respectively. Each current is represented as the finite sum of Dirac delta currents using Eq. 2.3 as $T_1 = \sum_n \delta_x^\alpha$ and $T_2 = \sum_m \delta_y^\beta$. The distance between two currents is defined as the

norm squared difference of the currents computed in the RKHS dual space given by

$$\begin{aligned} ||T_1 - T_2||^2_{W^*} &= < T_1 - T_2, T_1 - T_2 >_{W^*} \\ &= < T_1, T_1 >_{W^*} + < T_2, T_2 >_{W^*} -2 < T_1, T_2 >_{W^*} \\ &= \Big|\Big| \sum_n \delta^\alpha_x - \sum_m \delta^\beta_y \Big|\Big|^2_{W^*} \\ &= \sum_{n,n'} K^W(x_n, x_{n'}) \alpha^t_n \alpha_{n'} - 2 \sum_{n,m} K^W(x_n, y_m) \alpha^t_n \beta_m \\ &\quad + \sum_{m,m'} K^W(y_m, y_{m'}) \beta^t_m \beta_{m'} \end{aligned} \tag{2.6}$$

The image registration cost function for currents is defined as

$$C = ||\phi_* T_1 - T_2||^2_{W^*} + \gamma \Big|\Big| \sum_i v_{t_i}(x) \Delta \Big|\Big|^2_V \tag{2.7}$$

where ϕ is the transformation from the coordinate system of current T_1 to that of T_2 and ϕ_* is the differential of ϕ[9]. ϕ_* is also called the pushforward or total derivative of ϕ. The pushforward ϕ_* transforms the current T_1 into the coordinate system of the current T_2. Be careful, instead of deforming points in the images, the curve and surface currents are being deformed here. Both curve currents and surface currents can be represented by the Direct Delta current δ^α_x and the transformation of it is given by

$$\phi_* \delta^\alpha_x = \delta^{d_x \phi(\alpha)}_{\phi(x)} \tag{2.8}$$

where α is the tangent vector of a curve. For surface currents, the Eq. 2.8 becomes

$$\phi_* \delta^{u \times v}_x = \delta^{d_x \phi(u) \times d_x \phi(v)}_{\phi(x)} \tag{2.9}$$

where $u \times v$ is the normal of the surface[5].

2.2.2 Varifolds Framework

A varifold is a generalization of a current in the sense that the tangent vector of its representative momenta are not oriented. A varifold representation provides an advantage over a current representation for representing structures in which the orientation of the constitute line segments are unknown or difficult to discern. This is true for the current application in which the vessel trees may consist of disconnected line segments due to, for example, where a tumor or other pathology interrupts the vessel trees.

The image registration cost function for two curves represented by varifolds is similar to that for currents. Except for the term $< T_1, T_2 >_{W^*}$ in Eq. 2.7 is computed as:

$$\sum_{n,m} K^W(x_n, y_m) \frac{(\alpha_n^t \beta_m)^2}{|\alpha_n||\beta_n|} \tag{2.10}$$

instead of using

$$\sum_{n,m} K^W(x_n, y_m) \alpha_n^t \beta_m \tag{2.11}$$

as mentioned at www.deformetrica.org.

Therefore, we rewrite Eq. 2.7 for varifolds as:

$$\begin{aligned} ||T_1 - T_2||^2_{W^*} &= < T_1 - T_2, T_1 - T_2 >_{W^*} \\ &= < T_1, T_1 >_{W^*} + < T_2, T_2 >_{W^*} - 2 < T_1, T_2 >_{W^*} \\ &= \sum_{n,n'} K^W(x_n, x_{n'}) \frac{(\alpha_n^t \alpha_{n'})^2}{|\alpha_n||\alpha_n'|} - 2 \sum_{n,m} K^W(x_n, y_m) \frac{(\alpha_n^t \beta_m)^2}{|\alpha_n||\beta_n|} \\ &\quad + \sum_{m,m'} K^W(y_m, y_{m'}) \frac{(\beta_m^t \beta_{m'})^2}{|\beta_m||\beta_{m'}|} \end{aligned} \tag{2.12}$$

2.2.3 Representation of Diffeomorphism Flows

The second term in Eq. 2.7 is the discretized regularization term on the velocity of the transformation ϕ and is represented as $\int_0^1 ||v_t||_V^2 dt$ in continuous setting. Δ is the time interval. v_t is the velocity field at time t and can also be thought of as an element of a RKHS space. Therefore, it can be represented in terms of momenta

$$v_{t_i} = \sum_i K^V(., x_i(t))\alpha_i(t) \tag{2.13}$$

where $(x_i(t), \alpha_i(t))$ is the time varying momenta that parameterizes diffeomorphic transformation model.

Momenta are used to parametrize the velocity field v_t of the transformation ϕ in a similar way that momenta are used to parameterize the shapes of the objects, T_1 and T_2, to be registered. The relationship between the transformation ϕ and the time varying velocity field v_t is given by the O.D.E.

$$\frac{d}{dt}\phi_t^v(x) = v_t(\phi_t^v(x,t)) \tag{2.14}$$

where $t \in [0,1]$ and $\phi = \phi_1^v$. The time varying transformation ϕ_t^v is an isotopy between the identity transformation at time $t = 0$ (i.e., $\phi_0^v = Id$) and the transformation ϕ that maps T_1 into the shape of T_2 at time $t = 1$ (i.e., $\phi_1^v = \phi$). The superscript v on the transformation ϕ_t^v denotes the dependence of the transformation on the velocity field v_t. Note that varifolds cannot be used to represent the velocity field since the velocity field is a vector field in which the direction of the vectors are important. In the case of of parameterizing the velocity field with momenta, the magnitude of the vector no longer represents the length of a segment, but rather, it represents the velocity of the

transformation at certain point in time. The momenta representing the velocity field can be considered as vector weighted control points of the velocity field. Note that the location of the momenta are not fixed during the registration process and are free to move around during the registration process. The Deformetrica software was used to find the optimal location and direction for the control points of the velocity field for registration for the results generated for this paper [8].

2.3 Preprocessing and Sampling

2.3.1 Preprocessing

The Iterative Closest Point (ICP) [1] algorithm was used to rigidly align the shapes before registration. The main reason to use ICP is to remove the translational and rotational differences between the set of momenta locations of the moving and target shapes before nonrigid alignment.

2.3.2 Vessel Tree and Skeleton Extraction

For most radiation therapy interventions, the lung is imaged via computed tomography(CT). In a CT image, the vessels in a lung appear bright on a dark background. We used the Jerman et al. vesselness filter [12] to extract the vessel tree segmentation from a 3D CT image volume. In this method, the Hessian matrix is computed from the intensity values of the CT at each voxel location. Next, the eigenvalues are computed from the Hessian matrix. Tubular structures are then identified at voxel locations with one negligible eigenvalue and two similar non-zero negative eigenvalues. The skeletons extracted for 2D fundus images are generated

using a morphological thinning algorithm in ITK (www.itk.org). The vessel tree segmentation for 3D were then skeletonized using minimum cost paths[13]. The generated skeletons are located in discrete space in image coordinates, therefore line segments that represent the skeleton produces a piece-wise constant polygonal line with stair-step artifacts. A contour with stair-step artifacts gives a poor current and varifold representation since the tangent vectors from one line segment to the next do not vary smoothly. To over come this problem, we fit a second order polynomial to each vessel branch using regression. The fitted second order polynomial produced a smooth approximation to each branch that could be sampled at any resolution.

In this work, the momenta were sampled from the polynomial curves using units of pixels in 2D (voxels in 3D) in which the pixel (voxel) dimensions were isotropic. If branch length was not an multiple of the sampling period, we reduced the sample period enough to uniformly sampled the branch.

2.3.3 Lung Segmentation and Surface Triangularization

To extract lung surface, all fives lobes (right upper, right middle, right lower, left upper, and left lower) were delineated by individual trained by an experienced radiation oncologist using a commercial radiation oncology software suite (MIM Maestro v6.6.4, Cleveland, OH). Then the contours were converted to binary masks. We used the software iso2mesh(iso2mesh.sourceforge.net) to yield the trangularized mesh lung surface.

The visualization of the skeleton of the vessels in the lung and trangularized

mesh are implemented using Python and VTK(www.vtk.org).

CHAPTER 3
EXPERIMENTS

3.1 Phantom Data Experiments

3.1.1 Evaluation Methods

The registration results were evaluated using symmetric average closest distance(SACD) between two shapes. The average closest distance from one shape consisting of multiple curves to another is computed by taking each point in one shape and finding the closest point on the second shape. These distances are then averaged to get the average closest point distance. The average closest distance measured from one shape to another is often different than the average closest point distance computed when the roles of the two shapes are reversed. To mitigate this problem, we compute the symmetric average closest point distance which is the average of the distance compute from shape I_1 to shape I_2 and the distance computed from shape I_2 to shape I_1. The symmetric average closest point distance between two shapes I_1 and I_2 is given by

$$d(I_1, I_2) = \frac{1}{2}\left(\frac{1}{N_1}\sum_{y\in I_1}\min_{x\in I_2} d(x,y) + \frac{1}{N_2}\sum_{x\in I_2}\min_{y\in I_1} d(y,x)\right). \tag{3.1}$$

3.1.2 Sensitivity to the Number/Position of Momenta and the Kernel Size of the RKHS

One of the most important considerations for currents and varifolds registration of tree-like structures is (1) how to choose the number of the momenta, (2) how to choose the standard deviation λ_s of the Gaussian kernel K^W in Eq. 2.7 for the

shape and (3) how to choose the standard deviation λ_ϕ of the Gaussian kernel K^V in Eq. 2.13 for the deformation field.

To start to answer these questions, we designed an experiment that registered eight pairs of simple 2D branch structures (see Fig. 3.1) multiple times using different numbers momenta (see Fig. 3.2) and varying the shape kernel standard deviation λ_s. We kept the the deformation kernel standard deviation λ_ϕ fixed at 250 for this experiment. The registration error was computed for each registration and was used to evaluate the performance of each registration.

Figure 3.1 shows four of eight pairs of structures that were registered in this experiment. In this figure, the blue shape was registered to the red shape. Note that the bottom point of the vertical line segment for all of the red and blue structures start at the same location. Registration pairs 5, 6, 7 and 8 are not shown in this figure since they reverse the roles of the fixed and moving structures shown in panels a, b, c and d, respectively. The shapes in this figure were chosen to mimic a single simple branching structure from a real 3D pulmonary airway or vessel tree.

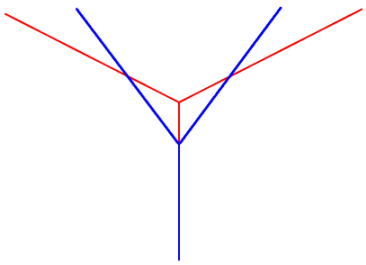

(a) Registration pair 1.

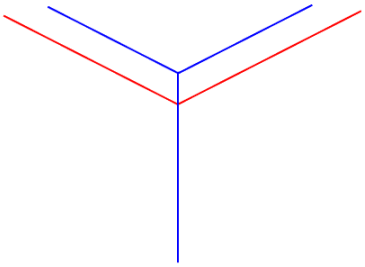

(b) Registration pair 2.

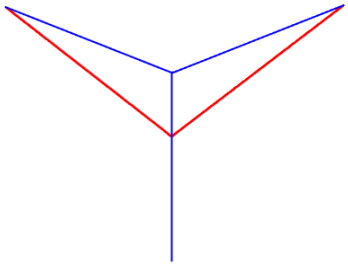

(c) Registration pair 3.

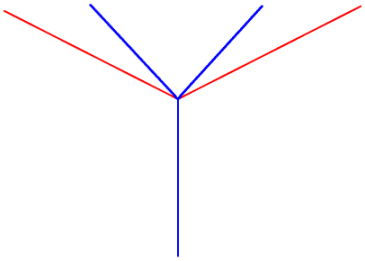

(d) Registration pair 4.

Figure 3.1: Simple 2D test structures used to characterize current- and varifold-based registration parameter selection. Red represents target structures and blue represents template structures. Registration pairs 5, 6, 7 and 8 are not shown in the figure; these registration pairs reverse the target and template structures shown in panels a, b, c and d, respectively. Note that the bottom point of the vertical line segment for all of the red and blue structures start at the same location.

Figure 3.2 shows how the momenta were positioned on one of the registration pairs. We similarly put the locations of momenta for other registration pairs.

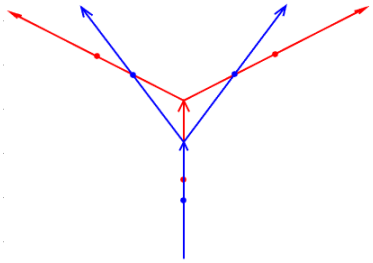

(a) Template and target shapes with 3 momenta.

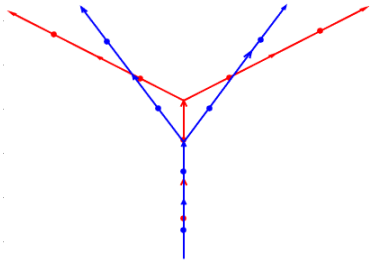

(b) Template and target shapes with 6 momenta.

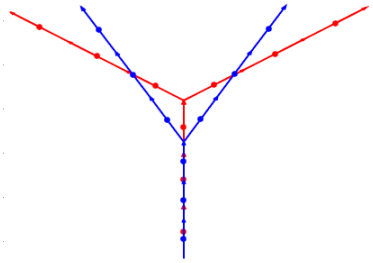

(c) Template and target shapes with 9 momenta.

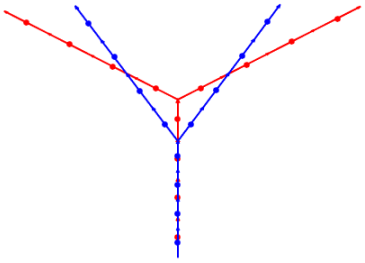

(d) Template and target shapes with 12 momenta.

Figure 3.2: Examples showing the number and placement of momenta.

This figure shows that the momenta were uniformly spaced along each of the branches for a total of 3, 6, 9 and 12 momenta for each shape. The case of three total momenta corresponds to the limiting case of one momentum per branch. We limited this experiment to 4 momenta per branch since we wanted to determine the fewest number of momenta required to accurately represent a branch. The reason for this is that the computation time increases as the number of momenta increases.

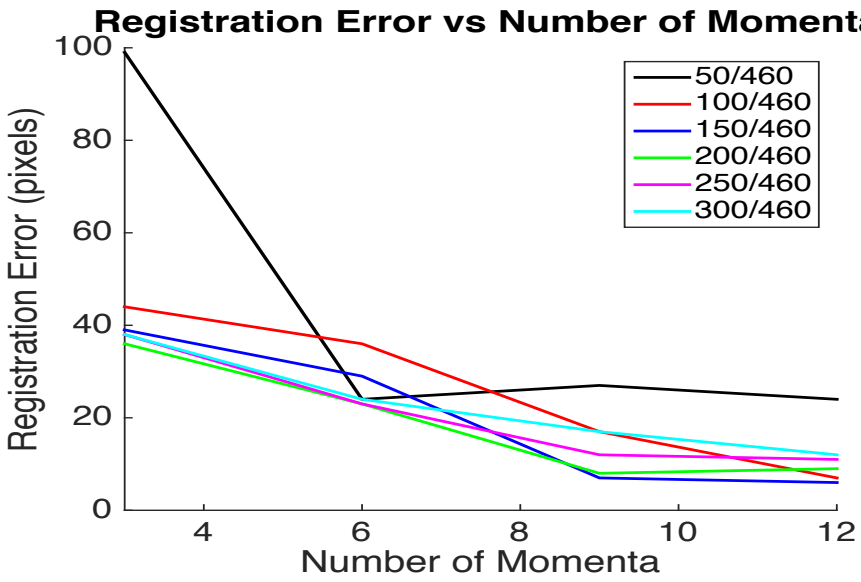

Figure 3.3: The effect of number of momenta on registration. For each kernel size, we use different number of momenta to represent the skeletons in the currents space and compute averaged registration error.

The graph in Fig. 3.3 shows the results of registering the eight pairs of branching shapes as a function of shape kernel standard deviation λ_s and the number of momenta used to parameterize the shapes. Each curve on the graph corresponds to a different shape kernel standard deviation λ_s. Each point on a curve is the average value of all eight registration results.

The graph in Fig. 3.3 shows that for this experiment, the lowest registration error is achieved for the shape kernel size of 150, which is $\lambda_s = 150$, which is $150/460 = 0.33$ times of the average branch size and for nine momenta. The registration error is similar for 9 and 12 momenta, but we prefer the smaller of these two numbers.

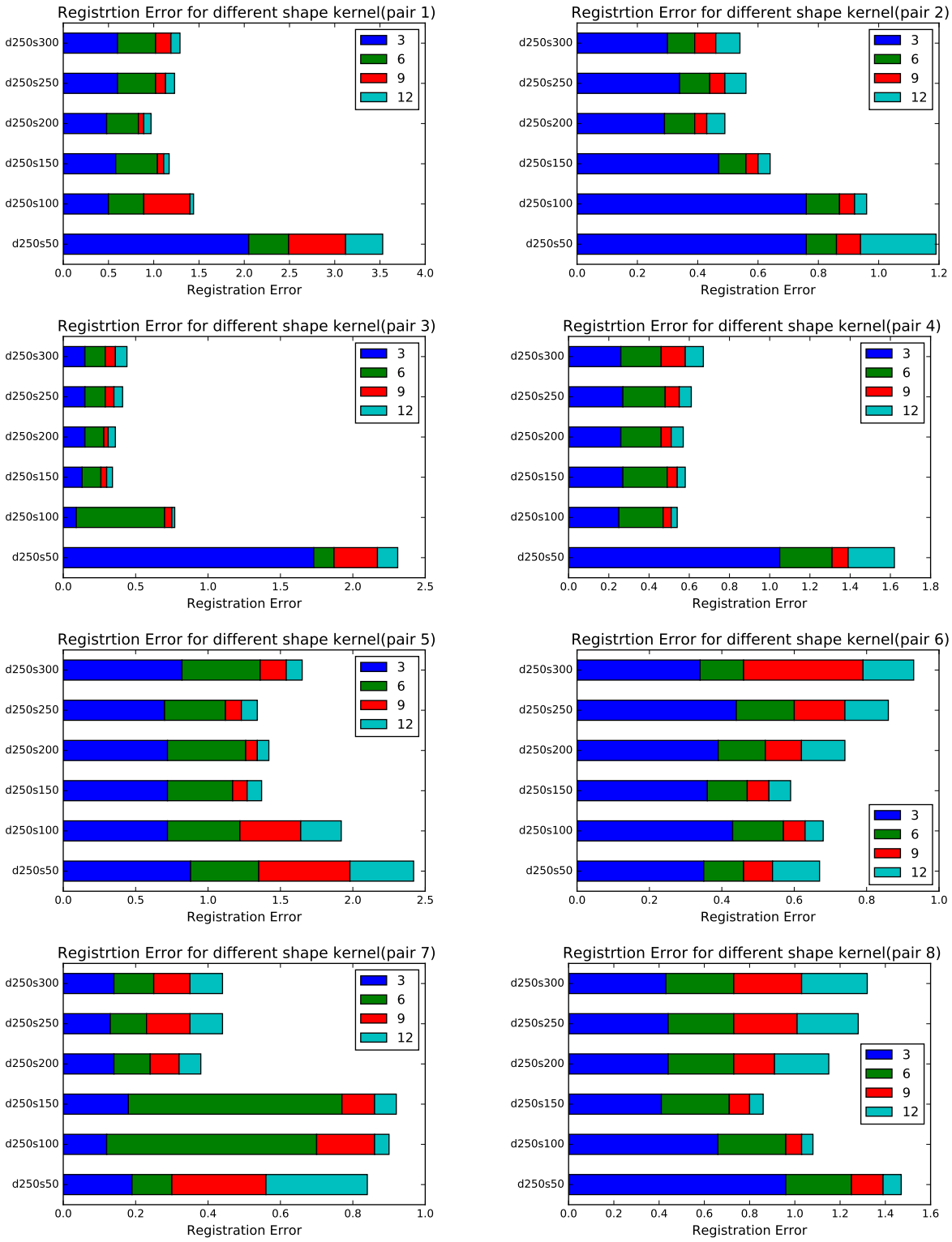

Figure 3.4: Registation error for each individual registration pair.

We also plot the results for each individual shape in Fig. 3.4, the x-axis is the registration error evaluated using SACD and the y-axis is different shape kernel size. We can see they are consistent with the averaged results as plotted in Fig.3.3.

This experiment suggests that one should use at least three momenta for a long branch without much curvature and a shape kernel size of 0.33 (1/3) times the average branch length.

The experiments were did so far on the 2D phantom shapes are based on the fact that the number of momenta used to represent the target and source template are the same. However, it hard to have the same number of samples for template and target shape for 3D real lung vessel trees. We will discuss about this more in later section. Therefore, another set of experiments we did using the eight pairs of shapes is we use different number of momenta to represent the source and target templates. Then we registered them using different kernel sizes and calculate the SACD registration error as we defined in Sec. 3.1.1 .

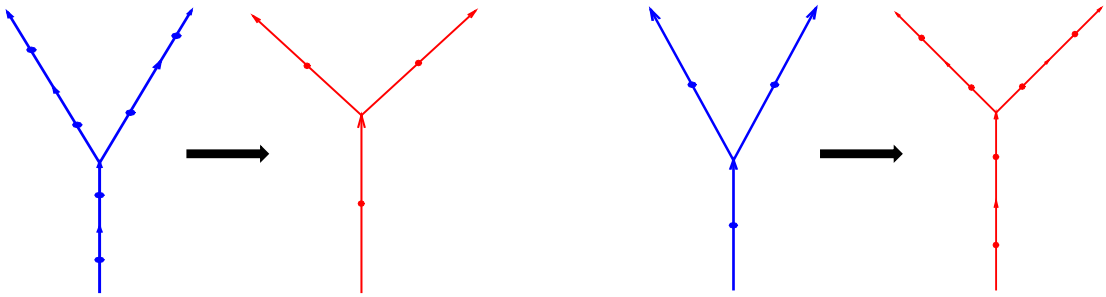

(a) High Resolution to Low Resolution. (b) Low Resolution to High Resolution.

Figure 3.5: Registration with variant resolution of target and source template.

As shown in Fig. 3.5, we use different number of momenta to represent the template and target shape, for example, we can use six momenta to represent the template shape and three momenta to represent the target shape as shown in Fig. 3.5a or we can use three momenta to represent the template shape and six momenta to represent the target shape as shown in Fig. 3.5b.

In Fig. 3.6, along the x-axis "Test3_6" means we use three momenta to represent the template(moving) shape and six momenta to represent the target(fixed) shape. "Test6_3" means the other way around, i.e. e use six momenta to represent the template(moving) shape and three momenta to represent the target(fixed) shape. We can see we achieve a smaller registration error when we use more momenta to represent template(moving) shape,especially, when the number of the momenta used to represent the shape is also small. When we sampled the shape finely, the registration

errors of these two cases were more similar.

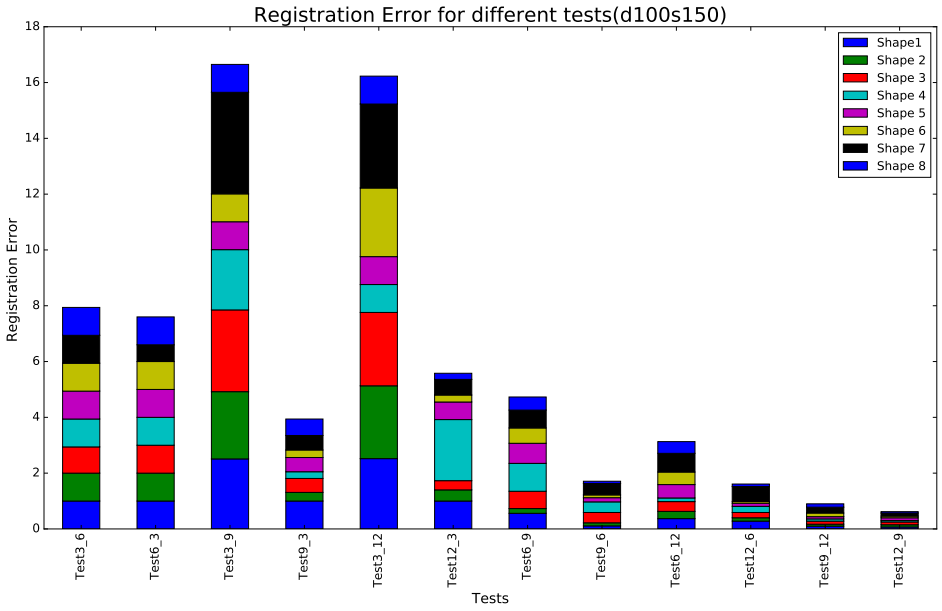

(a) Registration error with deformation kernel size 100, shape kernel size 150.

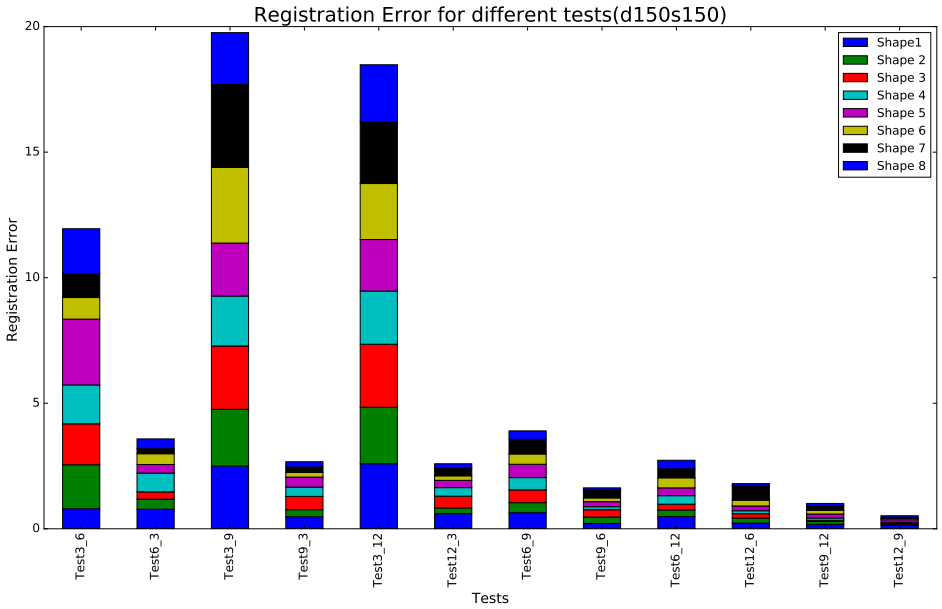

(b) Registration error with deformation kernel size 150, shape kernel size 150.

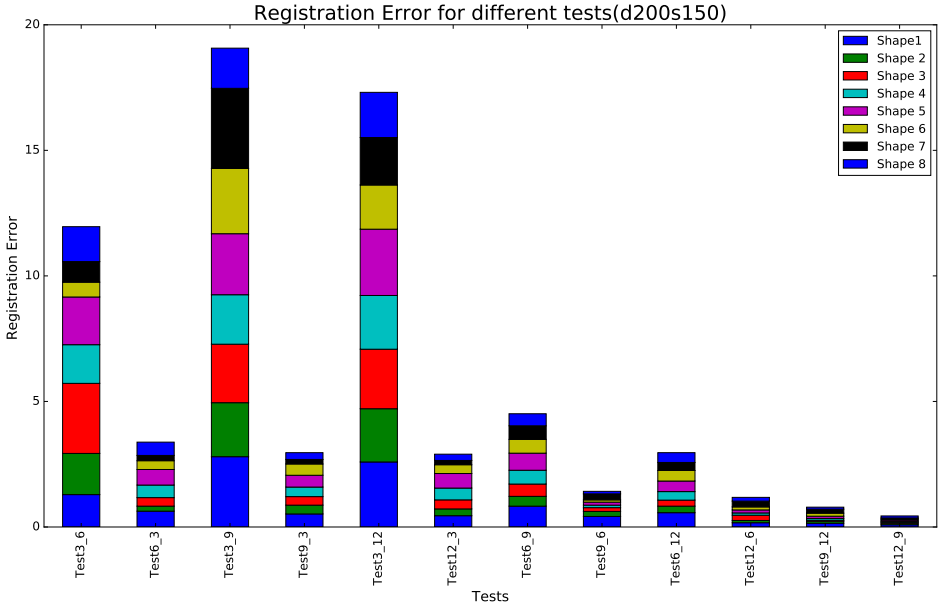

(c) Registration error with deformation kernel size 200, shape kernel size 150.

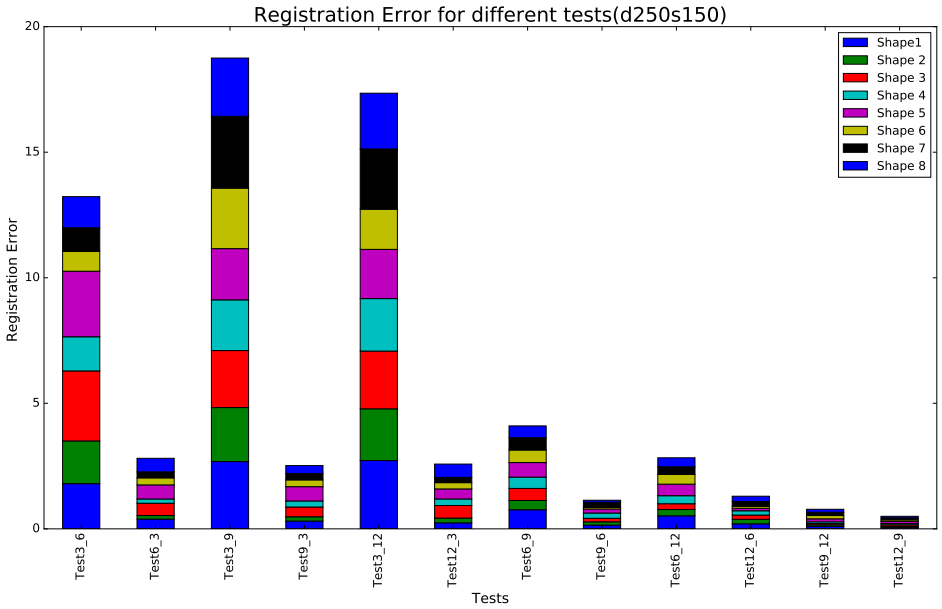

(d) Registration error with deformation kernel size 250, shape kernel size 150.

Figure 3.6: Registration error with variant resolution of target and source template. Test3_6 means we use 3 momenta to represent the template shape and 6 momenta to represent the target shape, Test6_3 means we use 6 momenta to represent the template shape and 3 momenta to represent the target shape and etc..

3.1.3 Simulated Vessel Tree Registration

In the next series of experiments, we used two simple 2D vessel trees (see Fig. 3.7a) that were were drawn to scale based on real 3D vessel trees extracted from CT images. The pixel dimensions for these vessel trees are 1 mm x 1 mm. In these experiments we varied the the deformation kernel standard deviation λ_ϕ, the shape kernel standard deviation λ_s and and the momenta sample period. The units for these variables are listed as pixels which are equal to 1 mm for these shapes.

Figure 3.7a shows two typical lung vessel branching structures with 31 branches and 15 branch points to be registered. The template (moving) vessel tree shape has 31 branches and 15 branch points. The minimum, maximum, mode and average (std dev) branch lengths were 7, 33, 9 and 13.1(6.18) pixels, respectively. The target vessel tree shape has 31 branches and 15 branch points. The minimum, maximum, mode and average (std dev) branch lengths were 6, 32, 8 and 13.8(6.48) pixels, respectively.

The vessel trees shown in 3.7a were registered 9*4*5 = 180 times with 9 different momenta sampling periods, 4 different shape kernel standard deviations λ_s and 5 different deformation kernel standard deviations λ_ϕ. Panels 3.7b-3.7d show the registration results when the sampling period equaled 1, 5 and 9 pixels, respectively, while keeping the shape kernel standard deviation λ_s fixed at 3 pixels and the deformation kernel standard deviation λ_ϕ fixed at 10 pixels. Result shown in Panel 3.7b was the best registration result out of the 180 registrations. Figure 3.7 demonstrates that the registration results got gradually worse as the sampling period increased.

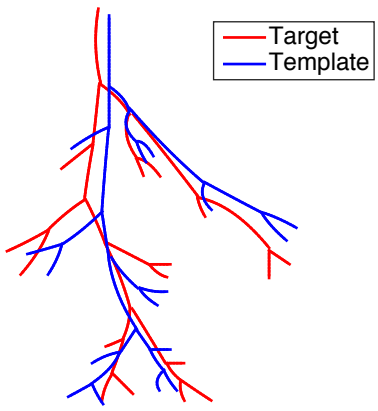

(a) Template (moving) and target vessel trees before registration. These shapes have the same scale as a subtree of a real 3D vessel tree.

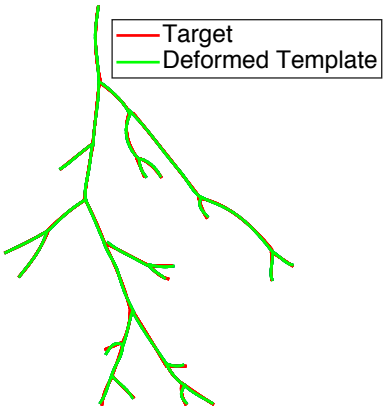

(b) Template and target shapes after registration: sample period = 1 pixel, deformation kernel size = 10 pixels, shape kernel size = 3 pixels.

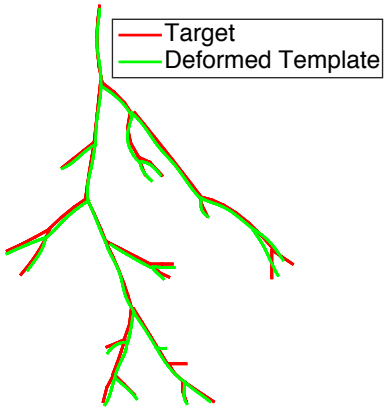

(c) Template and target shapes after registration: sample period = 5 pixel, deformation kernel size = 10 pixels, shape kernel size = 3 pixels.

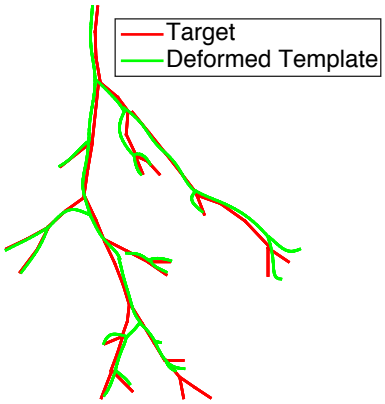

(d) Template and target shapes after registration: sample period = 9 pixel, deformation kernel size = 10 pixels, shape kernel size = 3 pixels.

Figure 3.7: Examples showing the number and placement of momenta.

Figure 3.8 shows the registration error as a function of the momenta sampling period and the shape kernel standard deviation λ_s. For these results the deformation kernel standard deviation λ_ϕ was fixed at 10 pixels. This figure shows that the best registration results were produced for the smallest sampling period.

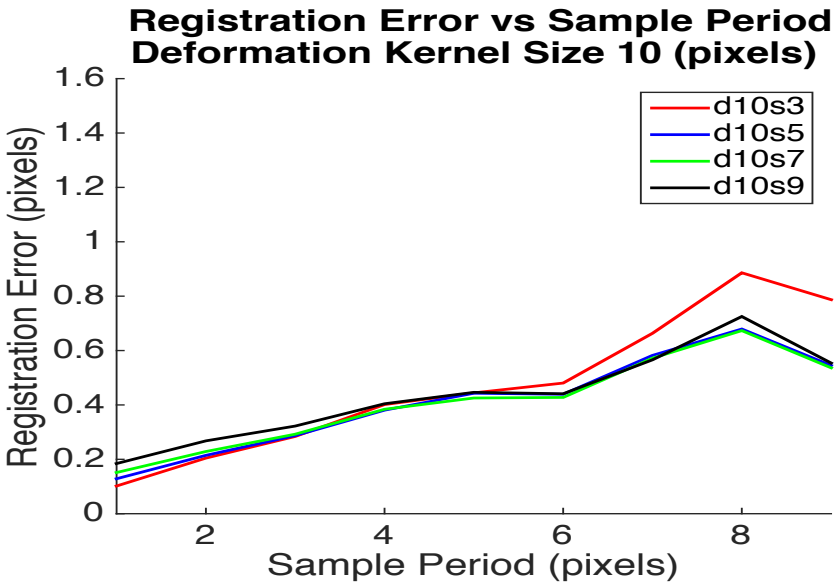

Figure 3.8: Registration error as a function of the momenta sampling period and the shape kernel standard deviation λ_s while keeping the deformation kernel standard deviation λ_ϕ was fixed at 10 pixels. The notation d10s3 corresponds to $\lambda_\phi = 10$ pixels and $\lambda_s = 3$ pixels.

Figures 3.9 and 3.10 shows the registration error as a function of the momenta sampling period and the deformation kernel standard deviation λ_ϕ. For these results the shape kernel standard deviation λ_s was fixed at 3 and 9 pixels, respectively. These figures show that the best registration results were produced for $\lambda_\phi = 10$ pixels which

is roughly the same size as the mode of the template and target branch lengths.

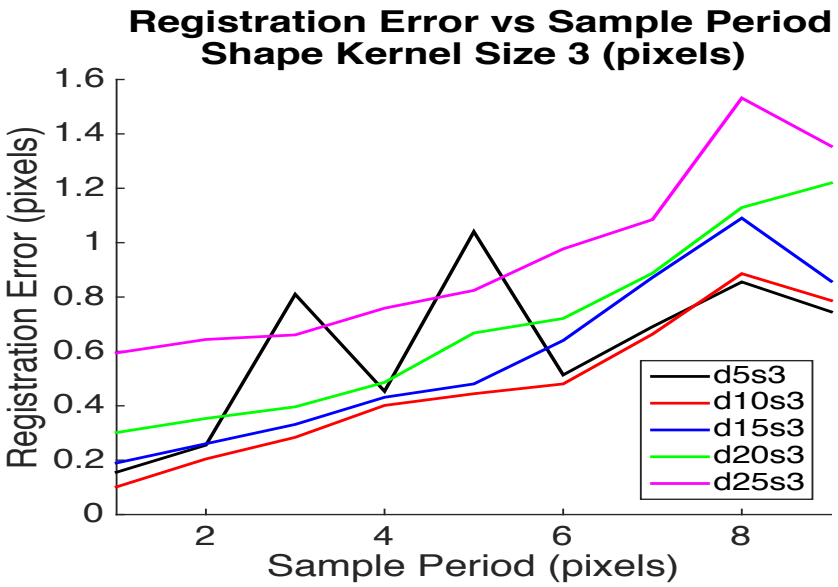

Figure 3.9: Registration error as a function of the momenta sampling period and the deformation kernel standard deviation λ_ϕ while keeping the shape kernel standard deviation λ_s was fixed at 3 pixels. The notation d10s3 corresponds to $\lambda_\phi = 10$ pixels and $\lambda_s = 3$ pixels.

Table. 3.1 shows that computation times increase as we decrease the deformation kernel size and decrease the momenta sampling period. The best registration results for the shapes shown in Fig. 3.7a were for sampling period 1 pixel, deformation kernel standard deviation 10 pixels and shape kernel standard deviation 3 pixels which took approximately 6 minutes to compute.

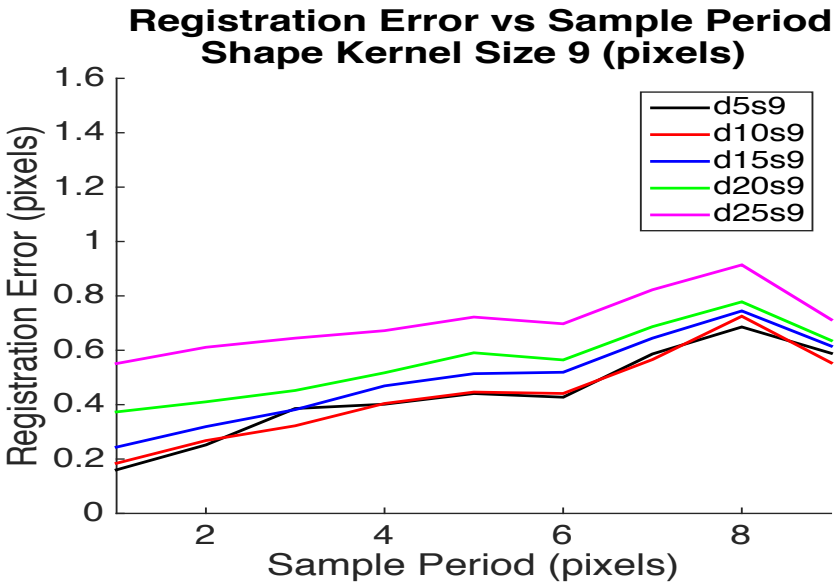

Figure 3.10: Registration error as a function of the momenta sampling period and the deformation kernel standard deviation λ_ϕ while keeping the shape kernel standard deviation λ_s was fixed at 9 pixels. The notation d10s3 corresponds to $\lambda_\phi = 10$ pixels and $\lambda_s = 3$ pixels.

3.1.4 Varifold Orientation Robustness

Based on the definitions of currents (See Eq. 2.1) and varifolds (See Eq. **??**), theoretically varifold representations should give better registration with unknown tangent orientations than currents. In order to learn more about the orientation robustness of the varifold representations, we did the following experiment. We used the same template and target shapes as in Section 3.1.3. We manually flipped the orientation of some branches in our template shape (see Fig. 3.11) to see how the registration results of currents- and varifold- representations differed. We sampled the

Kernel Size	d5s3	d10s3	d15s3	d20s3	d25s3
SP = 1	30m 47s	**6m 12s**	2m 31s	1m 33s	1m 9s
SP = 5	43m 47s	3m 34s	1m 9s	27s	20s
SP = 9	38m 25s	3m 17s	40s	22s	17s

Table 3.1: Computation time with respect to different deformation kernel standard deviations λ_ϕ and momenta sample periods for the experiments shown in Fig. 3.7. SP represent the momenta sampling period in units of pixels. The notation d5s3 corresponds to $\lambda_\phi = 5$ pixels and $\lambda_s = 3$ pixels. For this registration experiment, the shape kernel standard deviation λ_s did not have a noticeable affect on the computation time. Note that the smaller the momenta sampling period, the more momenta were used to parameterize the template and target shapes. Note that the smaller λ_ϕ, the more momenta were needed to parameterize the registration transformation.

template shape with sample period 1 and uses deformation kernel standard deviation $\lambda_\phi = 10$ pixels and a shape kernel standard deviation $\lambda_s = 3$ pixels.

First, we reversed the orientations of three branches on the template shapes and used currents and varifolds to represent our shape respectively.

The registration result of varifold representations is shown in Figure. 3.7b (a) and the registration result of current presentations is shown in Figure 3.11 (b). The region in the black circles in Figure. 3.7b (a) and (b) shows the three branches where we flipped the orientations of tangent vectors. We can see inside the black circle, two shapes don't align well with current representations while the varifolds-based registration give as a better result.

Similarly, we flipped seven branches of the template shape as shown inside the black circle in 3.11 (c) and (d). We can see the registration result of current representations in 3.11 (c) is bad inside the black circle, while the registration result of varifold representation 3.11 (d) keeps the same.

Therefore, we can see varifolds representation is more robust to orientations of tangent vectors as we expected. As we showed in this experiment, when we flipped some branch's orientations, the registration result for varifold representations are the same no matter how many branches's orientations are flipped while the registration result of current presentations are not.

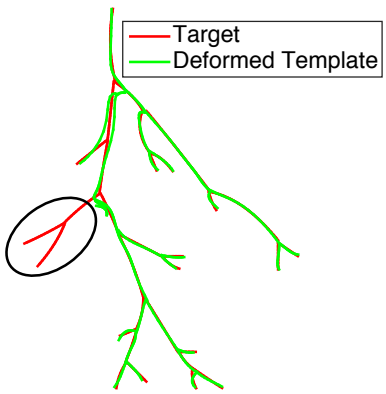

(a) Current registration result; 3 branches flipped orientation.

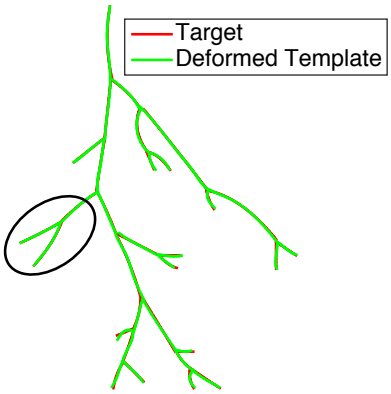

(b) Varifold registration result; 3 branches flipped orientation.

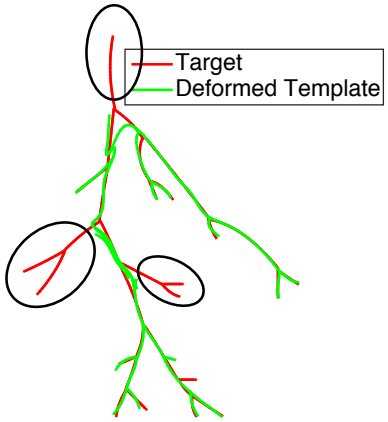

(c) Current registration result; 7 branches flipped orientation.

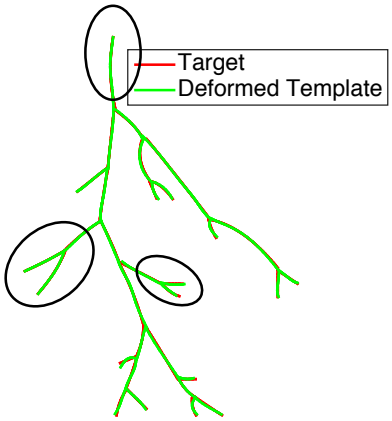

(d) Varfold registration result; 7 branches flipped orientation.

Figure 3.11: Registration results using current and varifold representations. The circles show the branches that had opposite tangent orientations between the template and the target. Notice that the current-based registration fails while the varifold-based registration does a good job of registering the shapes.

3.2 Real Data Varifolds- Based Registration – A Multi-resolution Framework

3.2.1 2D Fundus Images

The 2D fundus images data we are using in this thesis are obtained from the High-Resolution Fundus image database [2].

The fixed image is generated directly from the original fundus mask resampled to a smaller size which also had the intended consequence of interpolating the original binary (0 or 255) image to a range of intermediate values to produce a more realistic vesselness image (rather than a binary mask). The moving image is generated by deforming the fixed fundus image using elastix(http://elastix.isi.uu.nl) with a known B-Spline represented displacement filed. The size of the fixed and moving images are 1428×960. The original fixed and moving fundus images and extracted skeletons are shown in Fig. 3.12. The fixed structure has 447 branches and the minimum, maximum mode and average (std dev)branch lengths are 3, 64, 12 and 15 pixels, respectively. The moving structure has 404 branches and the minimum, maximum mode and average (std dev)branch lengths are 2, 55, 8 and 12 pixels, respectively.

In this experiment, we fully sampled the fixed and moving skeleton and only vary the shape and deformation kernel sizes.

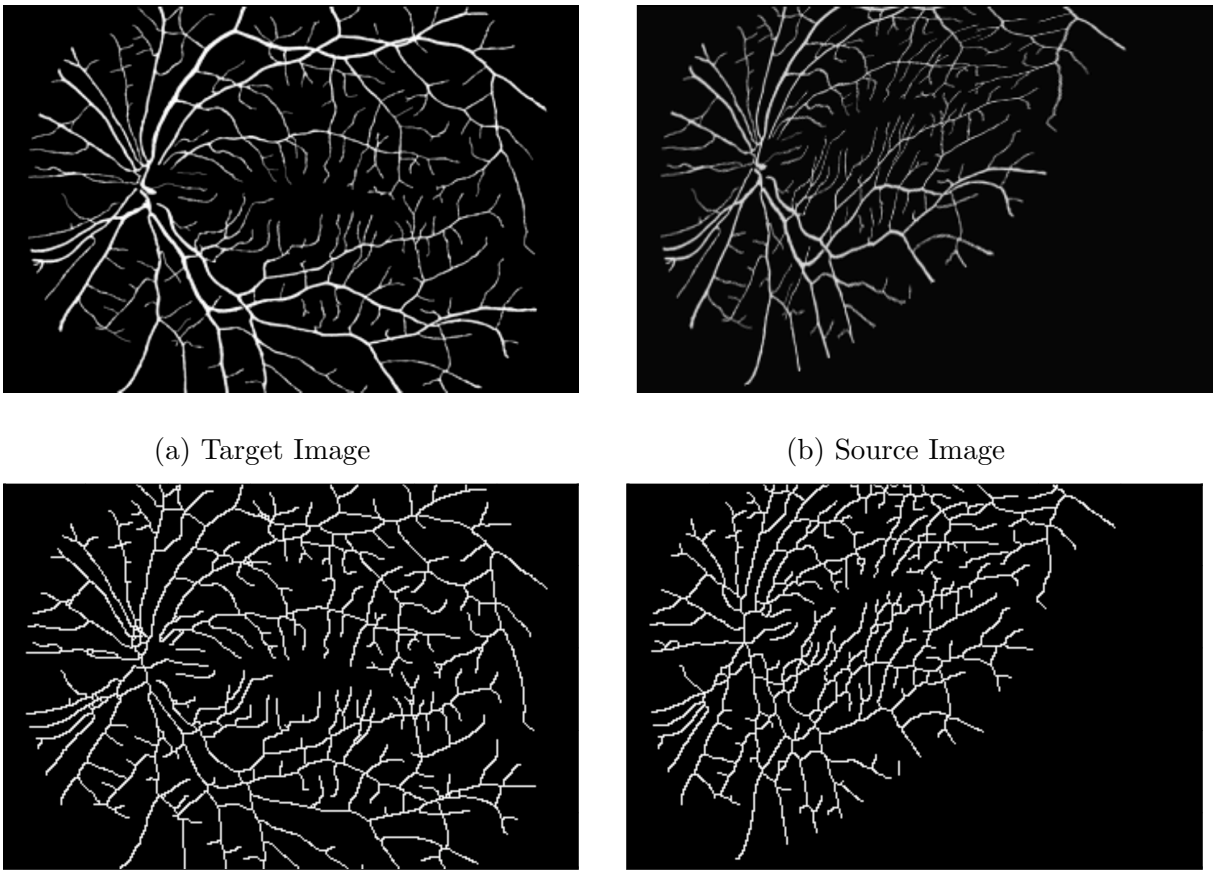

(a) Target Image

(b) Source Image

(c) Target Skeleton

(d) Source Skeleton

Figure 3.12: 2D Fundus images and extracted skeletons.

We started from a large deformation kernel size - 120 and shape kernel size - 50. Then reduce them separately. For deformation kernel size, we chose 120, 80, 40 and 20. For shape kernel size, we chose 50, 30, 15, and 5. We ran the algorithm using all combinations of the different deformation and shape kernel sizes and computed the SACD registration error as defined in 3.1.1.

In addition, we manually labeled ten corresponding landmarks at junction

positions of the fixed and moving vessels as shown in 3.13. The first five(red) were labeled at junctions of large branches while the last five(blue) were labeled at junctions of smaller branches. We computed the landmarks error for these ten landmarks and also computed the landmarks error for the "red" and "blue" landmarks separately to see how the deformation and shape kernel sizes affect the matching of branches with different length.

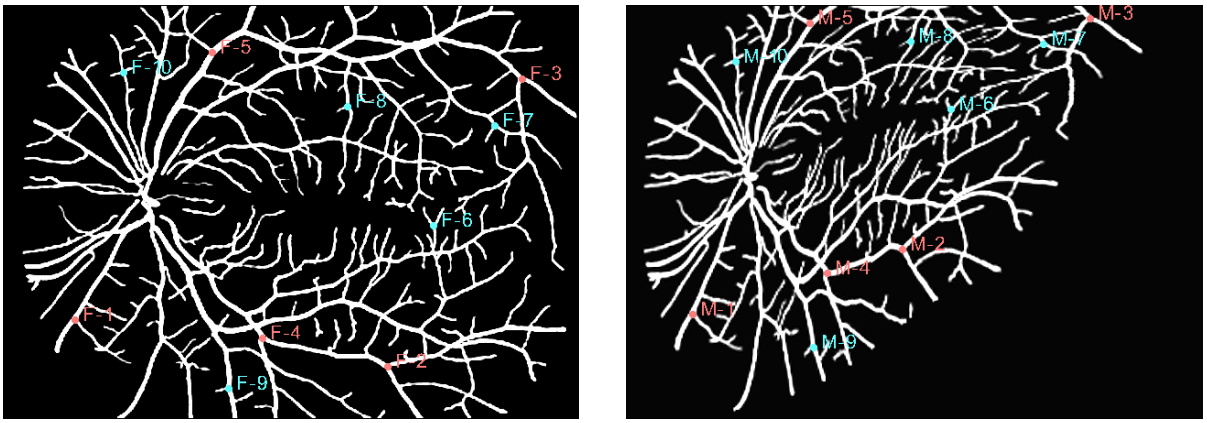

(a) Labeled Landmarks in Fixed Fundus Image

(b) Labeled Landmarks in Moving Fundus Image

Figure 3.13: Manually labeled landmarks in fundus images at junction positions.

Kernel Size	d120	d80	d40	d20
s50	1.22	1.24	1.31	1.44
s30	1.14	1.16	1.14	1.41
s15	1.22	1.06	0.91	1.12
s5	2.62	3.97	4.47	5.93

Table 3.2: SACD Registration error.

As we can see in Table. 3.2, the smallest registration error we got is when the deformation kernel size is 40 ans the shape kernel size is 15. Correspondingly, in Table. 3.3, the landmarks errors are much smaller when we have shape kernel size 15 at junctions of both short branches and long branches. There were no landmarks error for d20s15 because the deformations of some landmarks were too large and they were deformed outside the working domain.

We also notice the distance between landmarks error of longer branches and shorter branches are smaller when the shape kernel sizes are smaller. However, we can also learned from the Table. 3.3 the shape kernel size should not be too small when the dissimilarity between the two shapes is large at beginning.

For the experiments we did for phantom data, we learned that the shape kernel size should be around 1/3 of the averaged shape, which was not consistent with the conclusion of this experiment.

The reason is that the deformation of the phantom shapes and 2D simulated vessels are relative small comparing with this experiment and the structures in this case are more complex than the previous two.

Kernel Size	Combined Error	Combined Std	SmallBr Error	SmallBr Std	LargeBr Error	LargeBr Std
Before Reg	42.95	27.71	45.82	26.63	40.07	28.45
d120s50	10.75	7.51	13.71	7.75	7.80	5.94
d120s30	8.62	5.88	10.36	6.21	6.87	4.96
d120s15	3.05	1.10	3.47	0.83	2.65	1.18
d120s5	20.77	18.10	23.13	18.92	18.41	16.91
d80s50	11.55	8.84	15.70	9.43	7.39	5.75
d80s30	8.95	6.19	10.92	6.29	6.97	5.41
d80s15	3.21	2.14	3.13	1.51	3.29	2.62
d80s5	29.16	25.42	36.01	29.62	22.30	17.91
d40s50	17.55	13.74	22.66	14.82	12.45	10.29
d40s30	11.72	9.20	13.97	9.44	9.46	8.36
d40s15	3.39	2.43	3.42	2.03	3.36	2.78
d40s5	33.55	28.43	38.08	31.50	29.01	24.16
d20s50	28.37	18.12	31.18	19.17	25.60	16.55
d20s30	29.56	17.49	33.63	18.93	25.48	14.84
d20s15	–	–	–	–	–	–
d20s5	40.33	26.26	43.95	26.07	36.71	25.95

Table 3.3: Registration landmark errors.

Error Type	d120s50_d80s30	d120s50_d80s30 _d40s15	d120s50_d80s30 _d40s15_d20s5
Combined Error	9.05	3.47	0.93
Combined Std	6.55	2.42	0.88
SmallBr Error	10.75	3.81	0.71
SmallBr Std	6.45	1.53	0.36
LargeBr Error	7.35	3.76	1.14
LargeBr Std	6.20	3.03	1.15
SACD	1.11	0.97	0.77

Table 3.4: 2D Fundus images multi-resolution varifold-based registration errors in 2D.

Therefore, in order to get a better registration results, we proposed a multi-resolution strategy, we used larger deformation kernel size and shape kernel size first to perform a "affine-like" registration, which can align the shapes globally. Then we chose smaller deformation kernel size and shape kernel size to match the details of the structure.

As shown in Table. 3.4, the multi-resolution framework can improved the registration results, the smallest landmarks error is 0.93 and the smallest SACD is 0.77, while in Table. 3.2 and Table. 3.3, the smallest SACD is 0.91 and the smallest landmarks error is 3.05. Especially, the landmarks error improved a lot, which means we achieved a good matching correspondence.

We visualize the registration results as overlayed shapes in Fig. 3.14. We can see the multi-resolution framework can match the short branches better than the results with one single resolution.

(a) Overlayed skeletons before registration. In this experiment, we fully sample the skeletons.

(b) Overlayed skeletons after registration with deformation kernel size 20, shape kernel size 5(d20s5).

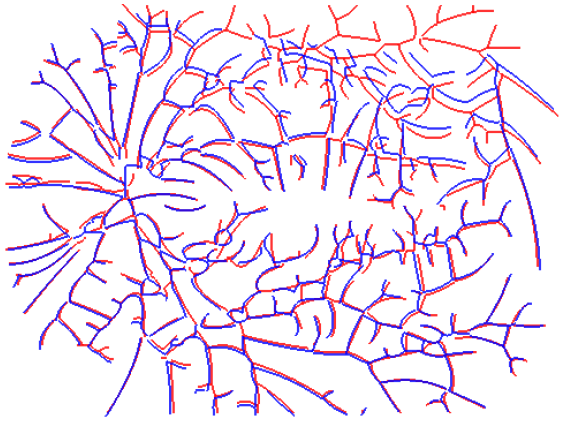

(c) Overlayed skeletons after registration with deformation kernel size 80, shape kernel size 15(d80s15).

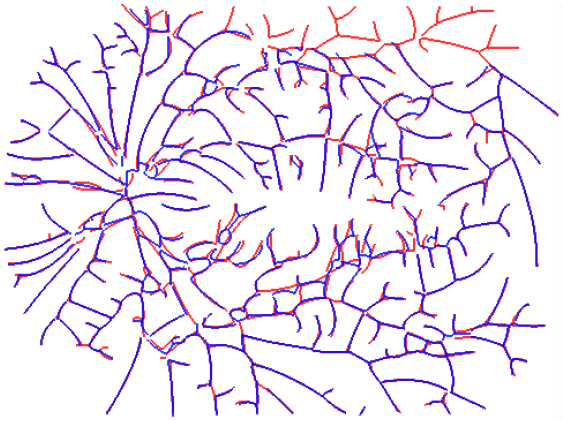

(d) Overlayed skeletons after registration with multi-resolution(d120s50_d80s30_d40s30_d20s15).

Figure 3.14: 2D Fundus images varifolds-based registration results with various deformation and shape kernel sizes.

3.2.2 3D Lung CT Images

Finally, we moved to the experiments of 3D real data. The data we used is a pair of baseline and mid-treatment computed tomography(CT) scans of human lungs which were acquired on a CT simulator(Philips Brilliance Big Bore, Fitchburg, WI) under IRB-approved protocols. The mid-treatment scan was taken 5 weeks later than the baseline scan was taken[11].

The size of the CT images we used in this experiment are $512 \times 512 \times 130$ voxel and the spacing along x, y, z each direction are 1.1719mm, 1.1719mm, 2mm.

We know each lung has five lobes, three at right and two at left. We can consider a lung as a complex shape that consist of five lobes different lobes and we register them with known correspondence. We still get a unique deformation, but the estimation of this deformation is constrained to match each pair of homologous objects as introduced in [8]. We make the registration more constrained, i.e. we math the right upper lobe to the right upper lobe, the left upper lobe to the left upper lobe and etc. as shown in Fig. 3.15. For this patient, the position of the tumor is at the right lower and middle lobe and these two lobes are collapsed together because of atelectasis, so we combined the masks of right middle lobe and right lower lobe and treated them as one object as shown in Fig. 3.15 in green.

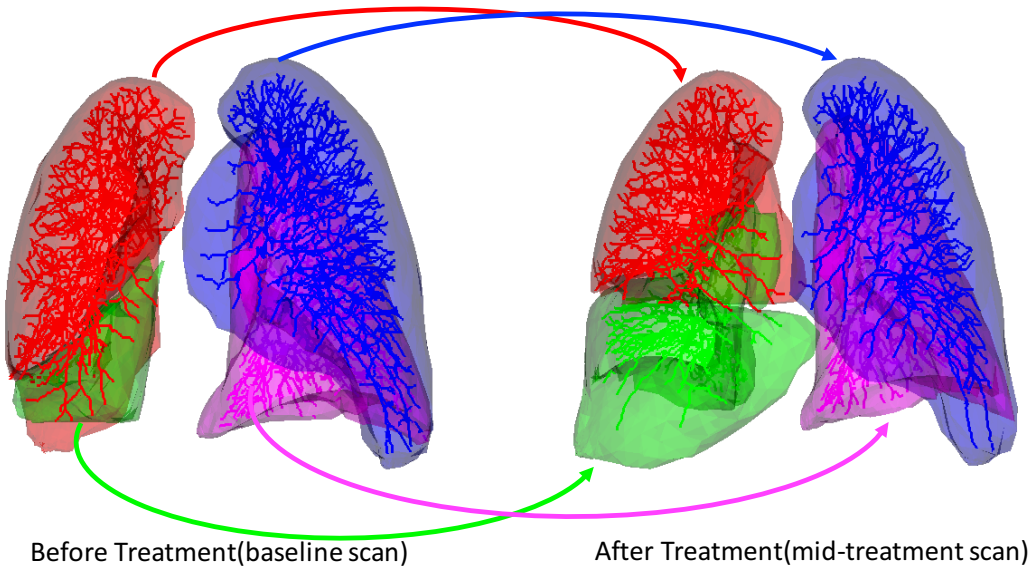

Figure 3.15: Extracted vessel skeleton and lung surface.

We segmented the lung vessels and lung surface first, then extracted the skeletons of the vessels and generated the triangular meshes of the lung surface as described in Section. 2.3.3 and Section. 2.3.2.

In stead of registering the whole lung, which would take longer time to run the algorithm, we registered the right upper lobe first. We registered the before treatment scan to after treatment scan. For the shape before treatment as shown in Fig. 3.16a in blue, the average and mode of branch length are 14.6mm and 7.2mm. For the shape after treatment as shown in Fig. 3.16a in red,the average and mode of branch length are 14.3mm and 5.2mm.

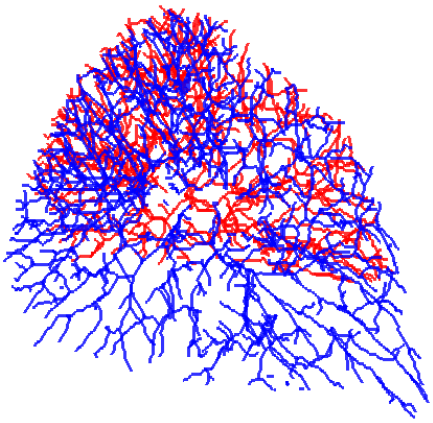

(a) Overlayed 3D skeletons before registration. This is the right upper lobe of a human lung.

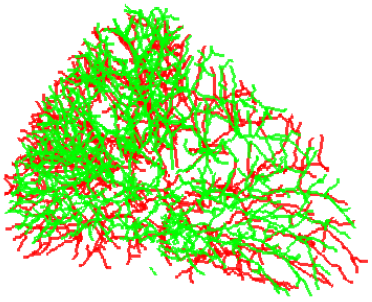

(b) Overlayed 3D skeletons after registration with deformation kernel size 80, shape kernel size 15.

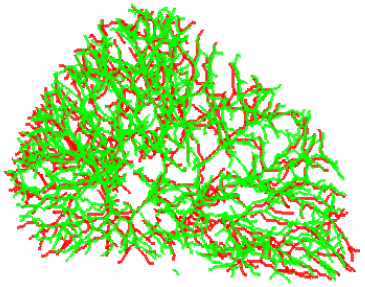

(c) Overlayed 3D skeletons after registration with deformation kernel size 50, shape kernel size 12, then followed by shape kernel size 5.

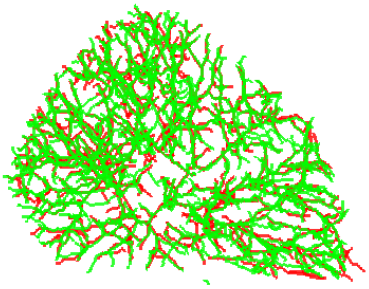

(d) Overlayed 3D skeletons after registration with multi-resolution framework. We use larger kernel sizes for both kernel first, then reduce both wisely.

Figure 3.16: 3D right upper lobe of real human lung varifolds-based registration results.

As the results we can see in Fig. 3.16, multi-resolution framework with appropriate parameters can improve the registration results. At the coarsest resolution, the shape kernel size should be around the averaged branch length of the shape in order to get a good pre-aligned, and the deformation kernel size should be relatively large, since we want a "affine-like" registration at the first resolution. Then, both of the kernel sizes should be reduced. However, remember the smaller the deformation kernel size, the more control points we need for the deformation field, this would increase the computation and the algorithm would run slower. We should reduce the deformetion kernel size wisely, as in Table. 3.3, different deformation kernel sizes with same shape kernel sizes can give similar registration, we should choose the larger one to reduce the computation. At the finest resolution, the shape kernel size and deformation kernel size should be near 1/3 of the average branch length and the average branch length.

We also registered the right upper lobe of the lung with varifold surface representation. Fig. 3.17a is the generated triangular meshes of the lung surface for the before treatment scan and Fig. 3.17b is the generated triangular meshes of lung surface for the after treatment scan. These triangular meshes were generated from the mask of the lung, which is a 3D image volume using the open source "iso2mesh" as mentioned in Sec. 2.3.3.

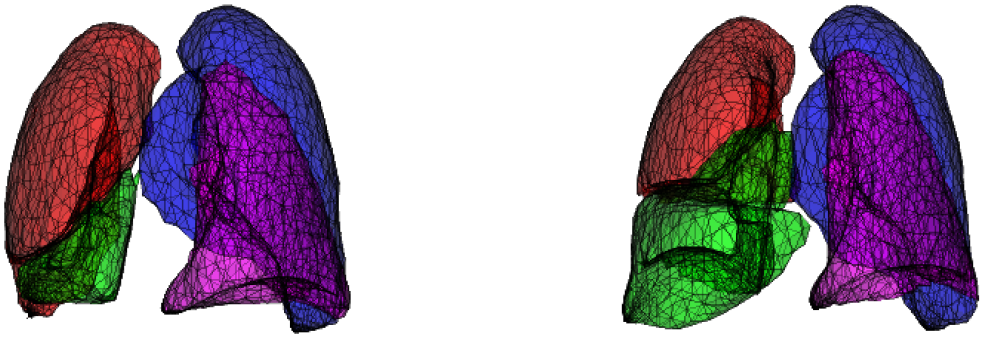

(a) Triangularized template lung surface of right upper lobe.

(b) Triangularized source lung surface of right upper lobe.

Figure 3.17: 3D Triangularized lung surface of right upper lobe.

The overlayed surface meshes before and after registrations are shown in Fig. 3.18. In Fig.3.18a, the red surface is the target shape and blue surface is the template shape. Same in Fig. 3.18, the red surface is the target shape and green surface is the deformed template shape. We can see the registration result is really good, they perfectly match. This result also came from a multi-resolution framework.

In Fig. 3.19, we register the whole lung using both lung vessels and surface information and run the algorithm with only two resolutions. In Fig. 3.19b is the deformed template shape and in Fig. 3.19b is the target shape. Comparing the deformed template shape with template shape we have in Fig. 3.15, we can see the result is acceptable even with two resolutions. Especially, for the right upper lobe.

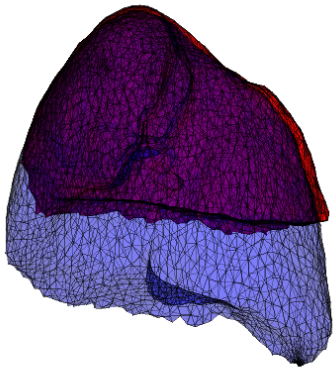

(a) Overlayed surface meshes of right upper lobe of template and target shapes before registration.

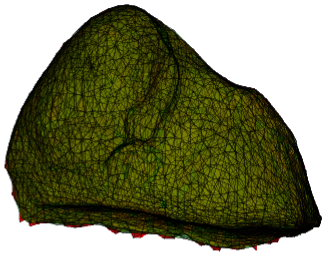

(b) Overlayed surface meshes of right upper lobe of template and target shapes after registration.

Figure 3.18: Registration results of meshes of right upper lobe of human lung.

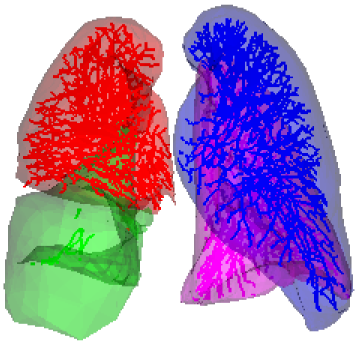

(a) Skeletons and meshes of deformed template whole human lung.

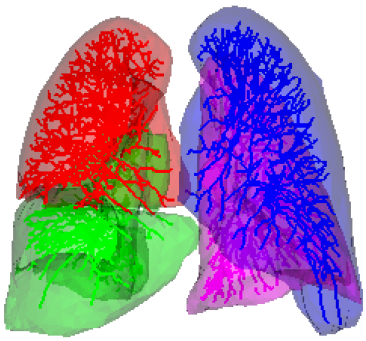

(b) Skeletons and meshes of target whole human lung.

Figure 3.19: Skeletons and meshes of 3D whole human lung after registration.

CHAPTER 4
CONCLUSION AND DISCUSSION

This thesis investigated the mathematical framework for registering 3D pulmonary vessel and surface using currents and varifolds. We constructed 2D experiments using simple tree shapes to measure the sensitivity of current and varifold registration to (1) the momenta sample period Δ, (2) the standard deviation λ_s of the Reproducing Kernel Hilbert Space (RKHS) Gaussian kernel used to represent shapes and (3) the standard deviation λ_ϕ of the RKHS Gaussian kernel used to parameterize the diffeomorphic registration transformation. For the experiments presented, we conclude that the best registration results for the simple phantom shapes were produced when (1) Δ was as small as possible, (2) λ_ϕ was close to the average of the template and target branch lengths and (3) λ_s was close to 1/3 of the average of the template and target branch lengths. We also showed that current- and varifold-based registration give equivalent results if the tangent orientations of the momenta are consistent between the moving shape and the target shape. We further showed that varifold-fold registration gives the same result for randomly oriented tangents. Then we registered real medical data-the 2D fundus images and 3D human lung CT images. For real medical data, the structure of the skeleton of the vessels are much more complex than the phantom shapes. Therefore we proposed a multi-resolution framework, which suggested to register the complex shape start from large deformation kernel size and choose the shape kernel size as the average branch length. Then wisely reduce them. At the finest resolution, the deformation kernel size shape should

be around the average branch length of the shapes and the shape kernel size should be around 1/3 of the average branch length. We also showed some registration results of surface representation and combined curve and surface representation, which give us very promising results. We will extend this work more in the future.

REFERENCES

[1] P. J. Besl and N. D. McKay. A method for registration of 3-D shapes. 14(2):239–256, 1992.

[2] Attila Budai, Jan Odstrcilik, Radim Kolar, Joachim Hornegger, Jiri Jan, Tomas Kubena, and Georg Michelson. A public database for the evaluation of fundus image segmentation algorithms. *Investigative Ophthalmology & Visual Science*, 52(14):1345–1345, 2011.

[3] K. Cao, K. Ding, G. E. Christensen, M. L. Raghavan, R. E. Amelon, and J. M. Reinhardt. Unifying vascular information in intensity-based nonrigid lung ct registration. In *4th International Workshop on Biomedical Image Registration*, LCNS 6204, pages 1–12. Springer, July 2010.

[4] Nicolas Charon and Alain Trouvé. The varifold representation of nonoriented shapes for diffeomorphic registration. *SIAM Journal on Imaging Sciences*, 6(4):2547–2580, 2013.

[5] Stanley Durrleman. *Statistical models of currents for measuring the variability of anatomical curves, surfaces and their evolution.* PhD thesis, Université Nice Sophia Antipolis, 2010.

[6] Stanley Durrleman, Xavier Pennec, Alain Trouvé, and Nicholas Ayache. Sparse approximation of currents for statistics on curves and surfaces. In *Medical Image Computing and Computer-Assisted Intervention–MICCAI 2008*, pages 390–398. Springer, 2008.

[7] Stanley Durrleman, Xavier Pennec, Alain Trouvé, Paul Thompson, and Nicholas Ayache. Inferring brain variability from diffeomorphic deformations of currents: an integrative approach. *Medical image analysis*, 12(5):626–637, 2008.

[8] Stanley Durrleman, Marcel Prastawa, Nicolas Charon, Julie R Korenberg, Sarang Joshi, Guido Gerig, and Alain Trouvé. Morphometry of anatomical shape complexes with dense deformations and sparse parameters. *NeuroImage*, 101:35–49, 2014.

[9] V. Gorbunova, S. Durrleman, P. Lo, X. Pennec, and M. de Bruijne. Curve- and surface-based registration of lung ct images via currents. In *Second International Workshop on Pulmonary Image Analysis*, pages 15–25, 2009.

[10] Matthias Guckenberger, Juergen Wilbert, Anne Richter, Kurt Baier, and Michael Flentje. Potential of adaptive radiotherapy to escalate the radiation dose in combined radiochemotherapy for locally advanced non–small cell lung cancer. *International Journal of Radiation Oncology* Biology* Physics*, 79:901–908, 2011.

[11] Christopher L Guy, Elisabeth Weiss, Nuzhat Jan, Leonid Reshko, Gary E. Christensen, and Geoffrey D. Hugo. The effect of atelectasis changes on mass and dose during lung radiotherapy. *Medical Physics*. (in press).

[12] Tim Jerman, Franjo Pernuš, Boštjan Likar, and Žiga Špiclin. Beyond frangi: an improved multiscale vesselness filter. In *SPIE Medical Imaging*, pages 94132A–94132A. International Society for Optics and Photonics, 2015.

[13] Dakai Jin, Krishna S Iyer, Cheng Chen, Eric A Hoffman, and Punam K Saha. A robust and efficient curve skeletonization algorithm for tree-like objects using minimum cost paths. *Pattern recognition letters*, 76:32–40, 2016.

[14] Robert McLachlan and Stephen Marsland. Discrete mechanics and optimal control for image registration. *Anziam Journal*, 48:1–16, 2007.

[15] Michael I Miller, Alain Trouvé, and Laurent Younes. Geodesic shooting for computational anatomy. *Journal of mathematical imaging and vision*, 24:209–228, 2006.

[16] Jan-Jakob Sonke and José Belderbos. Adaptive radiotherapy for lung cancer. In *Seminars in radiation oncology*, volume 20, pages 94–106. Elsevier, 2010.

[17] M. Vaillant and J. Glaunès. Surface matching via currents. In *Information Processing in Medical Imaging*, pages 381–392. Springer-Verlag, July 2005.

[18] Elisabeth Weiss, Scott P Robertson, Nitai Mukhopadhyay, and Geoffrey D Hugo. Tumor, lymph node, and lymph node-to-tumor displacements over a radiotherapy series: Analysis of interfraction and intrafraction variations using active breathing control (abc) in lung cancer. *International Journal of Radiation Oncology* Biology* Physics*, 82:e639–e645, 2012.